LITHOS 400-401 (2021) 106364

Contents lists available at ScienceDirect

LITHOS

journal homepage: www.elsevier.com/locate/lithos

Research Article

Geochemistry of the Yumen picrites-basalts from the Emeishan large igneous province: Implications for their mantle source, PGE behaviors, and petrogenesis

Jun-Hua Yao [a,b,c,f], Wei-Guang Zhu [a,*], Yan-Jun Wang [e], Hong Zhong [a,d], Zhong-Jie Bai [a]

[a] State Key Laboratory of Ore Deposit Geochemistry, Institute of Geochemistry, Chinese Academy of Sciences, Guiyang 550081, China
[b] Center of Deep Sea Research & Key Laboratory of Marine Geology and Environment, Institute of Oceanology, Chinese Academy of Sciences, Qingdao 266071, China
[c] Center for Ocean Mega-Science, Chinese Academy of Sciences, Qingdao 266071, China
[d] University of Chinese Academy of Sciences, Beijing 100049, China
[e] State Key Laboratory of Nuclear Resources and Environment, East China University of Technology, Nanchang 330013, China
[f] Guangdong Provincial Key Laboratory of Marine Resources and Coastal Engineering, China

ARTICLE INFO

Keywords:
Emeishan large igneous province
Yumen picrites-basalts
PGE
Olivine composition
Mantle peridotite

ABSTRACT

Olivine compositions are often used to infer the source lithology of basaltic rocks, but the effect of source melting conditions on olivine chemistry remains poorly studied. Here we present mineral chemistry, whole-rock major and trace elements, Sr—Nd isotopes, and platinum-group element (PGE) concentrations for high-Ti picritic-basaltic rocks from Yumen area. These data provide new constraints on the source lithology and petrogenesis of these high-Ti rocks in the Emeishan large igneous province (ELIP). The picrites have primitive compositional features (e.g., high $Mg^{\#}$ values, depleted Sr—Nd isotopic compositions, no PGE depletions and/or fractionations). Some basaltic rocks have negative Nb—Ta anomalies, enriched Sr—Nd isotopic compositions, and depleted and/or fractionated PGE contents, indicative of fractional crystallisation, variable degrees of crustal contamination, and magmatic sulfide segregation. Combined with published data for the ELIP, the compositions of the primitive magmas and 10000Zn/Fe and FC3MS ($FeO/CaO - 3 \times MgO/SiO_2$, all in wt%) values of the ELIP high-Ti picrites are similar to those of garnet peridotite-derived experimental melts. Based on the primitive magma compositions, the ELIP high-Ti melts could have been produced by mantle melting at 4.0–5.4 GPa and 1620–1660 °C, and started to crystallise olivine at 1410–1550 °C, based on the Al-in-olivine thermometer, which are higher temperatures than for mid-ocean ridge basalts and ELIP low-Ti magmas. The high-Ni and low-Mn olivine phenocrysts in the ELIP high-Ti samples crystallised from peridotite-derived, MgO-rich melts at high temperatures. Variations in the physicochemical source melting conditions was enough to explain the differences in olivine Ni and Mn contents in the ELIP high- and low-Ti picrites-basalts. Additionally, the almost constant Pd, Pt, and Rh contents with decreasing $Mg^{\#}$ values indicate intermediate partition behaviors in the ELIP magmas. No correlations exist between whole-rock $10{,}000 \times Pd/Yb$ and $Mg^{\#}$, $(Th/Nb)_N$, and $\varepsilon_{Nd}(t)$ values, implying that selective assimilation of crustal sulfur resulted in magmatic sulfide saturation. We propose that the ELIP high-Ti magmas were derived from a deep-sourced garnet peridotite, and experienced various igneous processes during ascent through the continental lithosphere to form different types of ELIP high-Ti basaltic rocks.

1. Introduction

Identifying the source lithology of picritic-basaltic rocks is important as it is a crucial factor to unravel their nature of mantle source and petrogenesis. Based on differences in bulk partition coefficients for some trace elements (e.g., Ni–Mn–Ca) between peridotite and pyroxenite, Sobolev et al. (2007) proposed that olivine crystallised from pyroxenite-derived melts (e.g., Hawaiian shield-stage tholeiites) have higher Ni and lower Ca and Mn contents than those from peridotite-derived melts (e.g., mid-ocean ridge basalts [MORBs]). Subsequently, this approach has been widely used to discriminate between peridotitic and pyroxenitic mantle sources for basaltic rocks, and several studies have proposed that

* Corresponding author.
E-mail address: zhuweiguang@vip.gyig.ac.cn (W.-G. Zhu).

https://doi.org/10.1016/j.lithos.2021.106364
Received 22 April 2021; Received in revised form 12 July 2021; Accepted 12 July 2021
Available online 19 July 2021

a pyroxenitic component could have an important role in the mantle source of some large igneous provinces (LIPs; e.g., Hawaii, Siberia, Karoo, and Emeishan; e.g., Sobolev et al., 2007; Kamenetsky et al., 2012; Heinonen and Fusswinkel, 2017; Howarth and Harris, 2017; Ren et al., 2017; Hole, 2018). However, the trace element contents of olivine phenocrysts are also affected by other factors, such as the pressure–temperature (*P–T*) conditions and degree of melting, and volatile (H_2O and CO_2) contents of the mantle source. The melt produced by high-degree melting of pyroxenite can have similar Mn/Fe ratios to peridotite-derived melts (Herzberg, 2011). The partition coefficients of Ni, Mn, and Ca in olivine can decrease with increasing *P–T*, melt MgO content, and volatile contents (H_2O and CO_2), respectively (Gavrilenko et al., 2016; Li and Ripley, 2010; Matzen et al., 2013, 2017; Yao et al., 2021). Therefore, before evaluating the role of a pyroxenitic source on olivine composition, the physicochemical effects of source melting should first be considered.

The Emeishan LIP (ELIP) has been well studied and is thought to have a mantle plume origin (e.g., Chung and Jahn, 1995; He et al., 2003; Xu et al., 2004; Zhong et al., 2011; Zhong and Zhu, 2006). However, the mantle source lithology of the ELIP remains controversial (e.g.,

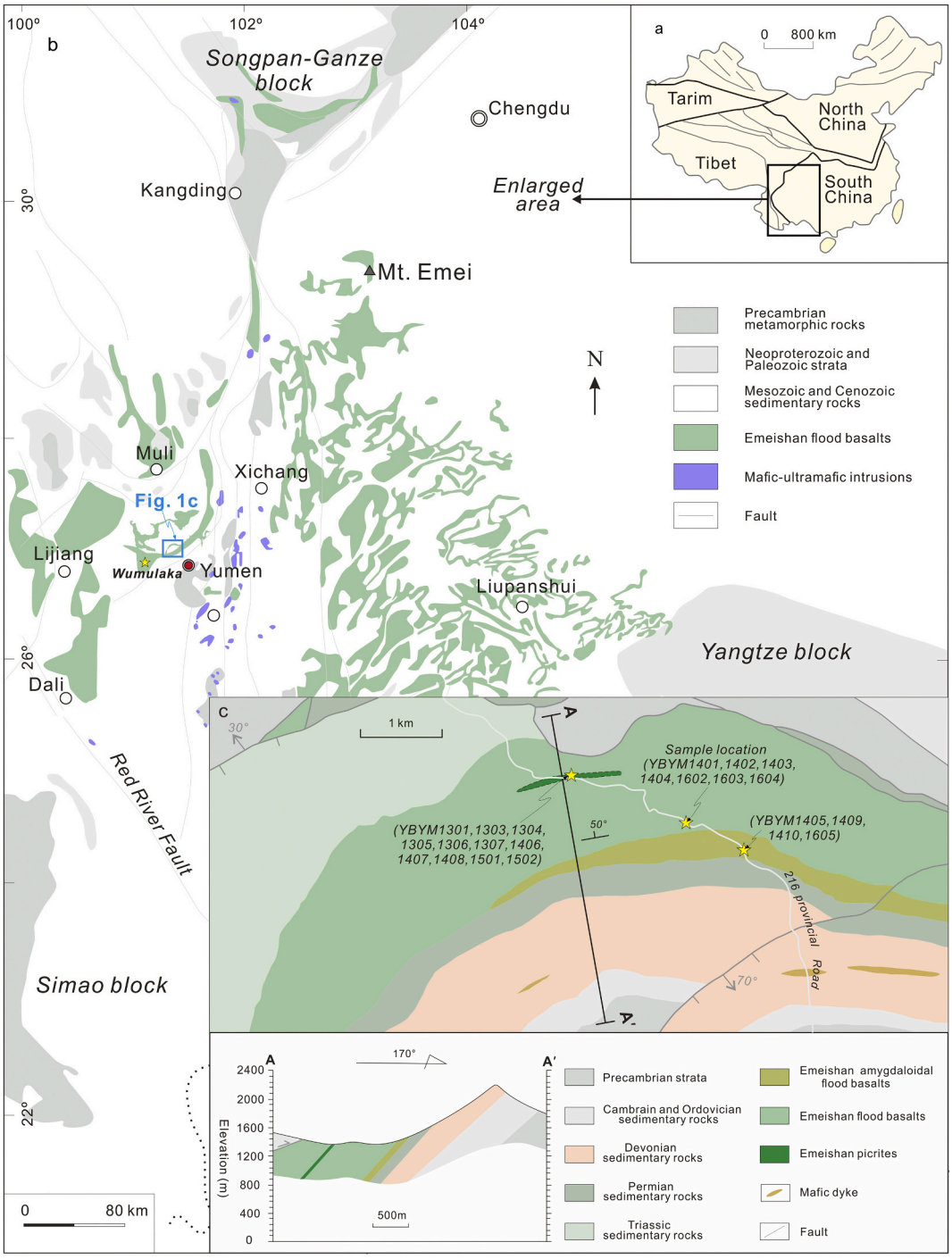

Fig. 1. (a) Schematic map showing the tectonic units of China and (b) the distribution of the Emeishan continental flood basalts and coeval mafic–ultramafic intrusions modified after Li et al. (2016). (c) Distribution of picrites and basaltic rocks in the Yumen area, southwest China, showing the sampling locations (modified after Yao et al., 2019).

Kamenetsky et al., 2012; Ren et al., 2017; Xiao et al., 2004; Xu et al., 2001; Xu et al., 2020; Yao et al., 2019; Yu et al., 2017). Compared with basalts, picrites have more primitive whole-rock and mineral compositions and are better for investigating the nature of the mantle source of LIPs (e.g., Chung and Jahn, 1995; Ellam, 2006; Li et al., 2012; Schaefer et al., 2000; Zhang et al., 2006). Based on normal $\delta^{18}O$ values, and high Mn/Zn and low Zn/Fe ratios of olivine in Emeishan high-Ti picrites (Yumen, Maoniuping, Tanglanghe, Wuguijing, and Wulongba), Yao et al. (2019) proposed that these rocks were mainly derived from mantle peridotite. However, these olivines also have high Ni and low Mn contents that can be used to infer derivation from pyroxenite-derived melt (e.g., Kamenetsky et al., 2012; Ren et al., 2017). Therefore, there are two different explanations for the origins of high-Ni and low-Mn olivines in the Emeishan high-Ti rocks: (1) The effect of source melting conditions on the olivine composition that crystallised from peridotite-derived melts; and (2) the olivine crystallised in pyroxenite-derived melts. In this study, we present whole-rock major and trace element (including platinum-group element [PGE]), Sr—Nd isotope, and mineral chemistry (olivine, Cr-spinel, and clinopyroxene) data for picritic-basaltic lavas from Yumen, which is a newly discovered outcrop of ELIP high-Ti rocks. These and previously published data for ELIP picrites and basalts are used to: (1) determine the relationship between the Yumen picritic-basaltic lavas and the ELIP; (2) constrain the lithology of the mantle source, including the effects of source melting conditions on olivine phenocryst composition; and (3) investigate the PGE partitioning and the cause of magmatic sulfide saturation in the ELIP. Finally, we present a model for the formation of high-Ti picrites and basaltic rocks in the ELIP and propose that the method based on trace elements in olivine to distinguish peridotite- and pyroxenite-derived melts needs to be further refined, which has significant implications for the contribution of pyroxenitic components to LIPs.

2. Geological background

Voluminous Permian basaltic volcanic rocks and mafic–ultramafic intrusions occur over an area of >250,000 km^2 in the western South China Block (i.e., the Yangtze and Cathaysia blocks that were amalgamated in the Neoproterozoic; Ali et al., 2005; Cawood et al., 2013; Shellnutt, 2014) from southwest China to northern Vietnam. These rocks form the ELIP (Fig. 1). The study area is located along the western margin of the Yangtze Block, which is bounded by the Tibetan Plateau to the west and separated from the North China Craton to the north by the late Palaeozoic–early Mesozoic Qinling–Dabie orogenic belt. The basement of the Yangtze Block consists of Archaean crystalline and high-grade metamorphic rocks, which is covered by post-Archaean, low-grade metamorphosed sedimentary sequences (Yan et al., 2003). In addition, abundant Neoproterozoic intrusive igneous rocks with granodioritic to mafic–ultramafic compositions are also widely distributed in this region (e.g., Li et al., 2002; Yao et al., 2018; Zhu et al., 2006, 2008).

The thickness of the Permian flood basalt sequence in the ELIP varies from ~5000 m in the west to several hundred metres in the east (Anh et al., 2011; Chung and Jahn, 1995; Xiao et al., 2004; Xu et al., 2001). The flood basalts were erupted from 263 to 257 Ma (Shellnutt et al., 2020; Zhong et al., 2020) and rest unconformably on upper Permian limestones, and they are unconformably overlain by uppermost Permian sediments in the east and west and Upper Triassic or Jurassic sediments in the central part of the ELIP (He et al., 2003). Some small mafic–ultramafic intrusions host magmatic Ni–Cu–PGE sulfide deposits, whereas world-class Fe–Ti–V oxide ore deposits are hosted by some large mafic intrusions (e.g., Bai et al., 2019; Shellnutt et al., 2011; Zhong et al., 2002; Zhou et al., 2008). The ELIP basalts are divided into two geochemical groups: high-Ti (TiO_2 > 2.5 wt% and Ti/Y > 500) and low-Ti (TiO_2 < 2.5 wt% and Ti/Y < 500; Xu et al., 2001, 2004; Xiao et al., 2004). Compared to low-Ti basalts, the ELIP high-Ti basalts are generally characterized by high whole-rock La/Sm and Sm/Yb ratios, and high Ni, low Mn contents in olivine. Many studies indicated that the ELIP high-Ti magmas maybe directly derived from low-degree partial melting of a deep mantle plume (e.g., Kamenetsky et al., 2012; Yao et al., 2019; Yu et al., 2017; Zhang et al., 2006). Considering the constant Pb isotope ratios in olivine-hosted melt inclusions with low-Ti to high-Ti compositions and some similar compositional features of major and trace elements to pyroxenite-derived melts, Ren et al. (2017) obtained a view that all ELIP basalts originated from a mantle pyroxenite. In contrast, based on the high Os concentrations and unradiogenic Os isotopic signatures in high-Ti basalts, Xu et al. (2007) suggested that the ELIP high-Ti magmas were likely derived from a sub-continental lithospheric mantle (SCLM). Yao et al. (2019) proposed that the contribution of recycled component for the ELIP high-Ti magmas maybe limited owing to the normal mantle-like olivine O isotopes and the olivine Zn/Mn and Zn/Fe ratios consistent with these from mantle peridotite-derived melts.

Picrite samples in the ELIP have been reported from only a few locations, including Yumen, Dali, Lijiang, and Muli in the west, and Jinping–Song Da in the south. The picrites and basaltic rocks in Yumen are newly discovered outcrops (Yao et al., 2019). The footwall and hanging wall of this volcanic sequence in Yumen are similar to those of the ELIP in the west. A picritic lava flow with a thickness of ~5 m is interbedded within a basaltic sequence (Fig. 1c). Yao et al. (2019) studied olivine phenocrysts and olivine-hosted Cr-spinel in the Yumen picrites, but whole-rock data for these rocks have not yet been obtained.

3. Sampling and analytical methods

3.1. Samples

In this study, seven picrites, six basalts, and five basaltic andesites (Hereafter, the term of "basaltic rocks" refers to the samples of basalts and basaltic andesites) were collected from the Yumen area, southwest China (Fig. 1c). Detailed latitudes and longitudes of sampling locations are listed in Table S1. The picrite samples contain abundant olivine phenocrysts with grain sizes of <50 μm to >2 mm across and occasional clinopyroxene phenocrysts. Euhedral to rounded olivine phenocrysts are partially serpentinised along with cracks and grain margins. Cr-spinel crystals that are a few tens of microns in diameter are enclosed in olivine phenocrysts or occur as isolated grains in the groundmass. The basaltic rocks consist of small, subhedral grains of clinopyroxene and plagioclase and are aphyric (Fig. S1).

3.2. Analytical methods

The compositions of olivine-hosted Cr-spinel, olivine, and clinopyroxene were determined by wavelength dispersive analysis using a JXA-8100 electron microprobe at Chang'an University, Xi'an, China. The analytical conditions were: 15 kV accelerating voltage, 20 nA beam current, 1 μm beam diameter, and peak counting times of 20–40 s for major elements and 40–60 s for minor elements.

Whole-rock major element contents of the Yumen samples were determined by X-ray fluorescence spectrometry (XRF) at the ALS Chemex Co. Ltd., Guangzhou, China. The analytical precision was better ±5%. Whole-rock trace element contents were determined with a Perkin–Elmer Sciex ELAN DRC-e inductively coupled plasma mass spectrometer (ICP–MS) at the State Key Laboratory of Ore Deposit Geochemistry (SKLODG), Institute of Geochemistry, Chinese Academy of Sciences (IGCAS), Guiyang, China. Powdered samples (50 mg) were dissolved in HF + HNO_3 acid in high-pressure Teflon bombs at ~190 °C for 48 h. Rhodium was used as an internal standard to monitor signal drift. The analytical precisions for most trace elements are generally better than ±10%.

Samples for whole-rock Sr—Nd isotope analysis were spiked and dissolved in Teflon bombs in a mixture of HF, HNO_3, and $HClO_4$ acid, and subjected to conventional two-step ion exchange chromatographic separation. The isotopic measurements were undertaken with a Thermo

Scientific Triton Plus multi-collector thermal ionisation mass spectrometer at the Institute of Geology and Geophysics, Chinese Academy of Sciences (IGGCAS), Beijing, China. The isotopic ratios were corrected for mass fractionation by normalising to $^{88}Sr/^{86}Sr = 8.375209$ and $^{146}Nd/^{144}Nd = 0.7219$, respectively. The international standards NBS-987 and JNDI were analysed to evaluate data quality. The measured values for the NBS-987 Sr and JNDI Nd standards were $^{87}Sr/^{86}Sr = 0.710246 \pm 0.000015$ ($n = 5$; 2 SD) and $^{143}Nd/^{144}Nd = 0.512114 \pm 0.000012$ (n = 5; 2 SD), respectively. The United States Geological Survey standard BCR-2 yielded $^{87}Sr/^{86}Sr = 0.705042 \pm 13$ (2σ) and $^{143}Nd/^{144}Nd = 0.512632 \pm 8$ (2σ). These values are identical to the recommended values for this standard.

The concentrations of PGEs were determined by isotope dilution (ID)–ICP–MS using an improved digestion technique, whereby sealed beakers were placed in stainless steel pressure bombs. Powdered samples (8–10 g) were dissolved in HF acid in customised 120 mL PTFE beakers on a hotplate. The dried residues were then digested in HF + HNO_3 acid in stainless steel pressure bombs at 190 °C for ~48 h. The solutions were analysed with an ELAN DRC-e ICP–MS instrument. The detection limits are <0.02 ppb for Pt and Pd, and < 0.01 ppb for Ir, Ru, and Rh.

4. Results

4.1. Mineral chemistry

The chemical compositions of Cr-spinel inclusions and olivine and clinopyroxene phenocrysts in the Yumen and Wumulaka picrites are listed in Table S2. Based on the classification of Cr-spinel using Ti/Al ratios following Yao et al. (2019), the picrites from the Yumen, Wumulaka, and Yongsheng areas are classified as being of the high-Ti group (molar 10Ti/Al > 0.5). Olivine phenocrysts in the Yumen picrites, along with olivine data from Yao et al. (2019), have Fo = 77–92 (Fo = 100 Mg/[Mg + Fe^{2+}]), and higher Ni and lower Mn and Ca contents (1790–3590 ppm Ni, 850–2610 ppm Mn, and 1640–2540 ppm Ca) relative to ELIP low-Ti picrites (Dali and Binchuan areas). The data exhibit positive Ni–Fo, negative Mn–Fo, and no Ca–Fo correlations. Clinopyroxene phenocrysts in the Yumen picrites have compositions similar to augite with $Mg^{\#}$ = 78–86 (100 Mg/[Mg + Fe^{T}]), and have higher TiO_2 contents and lower $Mg^{\#}$ values and CaO contents than those in the low-Ti picrites (Fig. S2).

4.2. Major and trace elements

Whole-rock major and trace element data for the Yumen volcanic rocks are listed in Table 1. The studied volcanic rocks comprise three rock types: picrite, basalt, and basaltic andesite (Fig. 2). The picrites contain 19.7–21.6 wt% MgO, 8.1–8.6 wt% Al_2O_3, 1.8–2.1 wt% TiO_2, and 8.4–10.3 wt% CaO. The ELIP high-Ti picrites have lower Al_2O_3 and higher TiO_2 contents than the ELIP low-Ti picrites. The basalts contain 5.6–8.8 wt% MgO, 5.5–12.5 wt% Al_2O_3, 2.2–3.6 wt% TiO_2, and 6.7–12.1 wt% CaO. With decreasing MgO contents, CaO decreases and Al_2O_3 increases. Whole-rock Ni contents of the Yumen basaltic rocks are lower than those in the picrites (Fig. S3).

Chondrite-normalised rare earth element (REE) patterns of the Yumen volcanic rocks are shown in Fig. 3a. The samples have uniform, almost linear REE patterns with enrichments in light REEs relative to heavy REEs. The picrites have lower REE contents than the basalts and basaltic andesites, which can be explained by the latter having a more fractionated parental magma. Primitive-mantle-normalised patterns of some immobile incompatible trace elements are shown in Fig. 3b. The Yumen picrites and basalts have ocean island basalt (OIB)-like patterns (e.g., enrichments in light REEs and small positive Nb—Ta anomalies), which are similar to other ELIP high-Ti picrites (e.g., Yongsheng). The high-Ti picrites have higher incompatible trace element contents and steeper patterns than the low-Ti picrites. Negative Nb—Ta anomalies are exhibited by some of the basaltic andesites from Yumen.

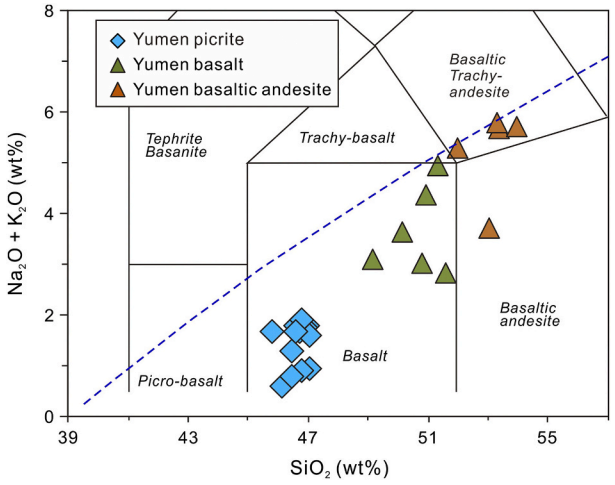

Fig. 2. Total alkalis ($Na_2O + K_2O$)–silica (SiO_2) (TAS) diagram for the picrites and basaltic rocks in the Yumen area.

4.3. Sr—Nd isotopes

Whole-rock Sr—Nd isotope data for the Yumen volcanic rocks are listed in Table 2. Calculated initial $\varepsilon_{Nd}(t)$ (t = 260 Ma) values and $(^{87}Sr/^{86}Sr)_i$ ratios for the Yumen picrites vary from +2.8 to +3.4 and from 0.70410 to 0.70445, respectively. Unlike the ELIP low-Ti picrites that have a wide range of Sr—Nd isotopic compositions (e.g., $\varepsilon_{Nd}(t) = -2.3$ to +7.0), the ELIP high-Ti picrites (Yumen, Wumulaka, and Yongsheng) have a limited range of Sr—Nd isotopic compositions (e.g., $\varepsilon_{Nd}(t) = +1.4$ to +4.0) and plot in the depleted mantle field. Initial $\varepsilon_{Nd}(t)$ and $(^{87}Sr/^{86}Sr)_i$ values of the Yumen basalts and basaltic andesites vary from −2.2 to +2.0 and from 0.70488 to 0.70573, respectively. The Sr—Nd isotope data for the Yumen basaltic rocks exhibit a negative correlation that trends towards the crust field (Fig. 4).

4.4. Cu, Ni, and PGE data

Whole-rock chalcophile element (Cu, Ni, and PGEs) concentrations of the Yumen volcanic rocks are listed in Table 3. Primitive-mantle-normalised patterns for Ni–PGE–Cu of the Yumen volcanic rocks are shown in Fig. 5. The Yumen picrites are characterized by unfractionated PGE patterns, but exhibit pronounced negative Ir anomalies relative to Ru. The Ni–PGE–Cu patterns are similar for the ELIP high- and low-Ti picrites. However, the Yumen basalts and basaltic andesites have fractionated PGE patterns with enrichments in PPGE (Pt and Pd) relative to IPGE (Ir and Ru), and some samples also exhibit negative Pt—Pd anomalies relative to Cu that are indicative of PGE depletion.

5. Discussion

To make best use of our new, but limited, geochemical data for the Yumen picrites and basalts, and constrain the mantle source and petrogenesis of the ELIP, we compiled whole-rock data for ELIP picrites and basalts with SiO_2 < 52 wt% and MgO > 4 wt%. These samples were divided into high-Ti (whole-rock Ti/Y > 500) and low-Ti groups (whole-rock Ti/Y < 500; Table S3).

5.1. Relationship between the Yumen picrites and basalts and the ELIP

The whole-rock major and trace element and Sr—Nd isotopic compositions, as well as the phenocrysts, of the Yumen picrites are similar to those of the ELIP high-Ti picrites (Figs. 3–4 and S2–S3). Their Sr—Nd

Table 1
Whole-rock major and trace element data for the Yumen volcanic rocks.

	YBYM1305	YBYM1406	YBYM1407	YBYM1408	YBYM1411	YBYM1501
	Picrite	Picrite	Picrite	Picrite	Picrite	Picrite
SiO_2	43.20	42.90	42.10	43.80	43.67	42.46
TiO_2	1.92	1.89	1.94	1.86	1.83	1.87
Al_2O_3	7.92	7.73	7.99	7.92	7.92	8.05
$Fe_2O_3^T$	12.98	13.40	13.52	13.58	13.14	13.40
MnO	0.17	0.19	0.19	0.18	0.18	0.20
MgO	18.45	18.80	18.00	19.20	18.75	17.80
CaO	8.56	8.33	9.36	8.27	8.22	9.22
Na_2O	0.62	0.64	0.39	1.13	1.02	0.54
K_2O	0.23	0.19	0.15	0.53	0.44	0.17
P_2O_5	0.17	0.16	0.16	0.17	0.16	0.16
LOI	5.48	6.07	5.82	3.13	4.13	5.68
Total	99.70	100.30	99.62	99.77	99.46	99.55
Sc	23.1	25.2	27.0	24.2	31.3	28.9
V	292	263	276	253	277	261
Cr	1541	1220	1260	1190	1314	1790
Co	74.0	80.3	81.3	83.5	81.7	88.8
Ni	831	591	597	585	853	1116
Cu	81.9	67.2	108	106	142	105
Zn	88.4	77.9	81.7	77.3	101	104
Ga	13.0	13.4	14.8	14.3	15.1	15.4
Rb	7.84	8.78	6.97	12.2	12.9	7.96
Sr	120	118	140	314	254	115
Y	15.4	16.2	17.4	16.8	16.4	16.4
Zr	123	124	132	129	130	126
Nb	15.9	15.8	16.4	16.3	16.5	16.4
Cs	0.26	0.53	0.34	0.28	0.37	0.33
Ba	78.8	53.8	60.1	184	168	65.6
La	15.4	16.3	16.6	17.0	17.1	15.3
Ce	36.4	38.0	39.9	40.0	41.4	35.3
Pr	4.59	4.77	4.98	5.03	5.20	4.56
Nd	20.7	19.5	21.3	21.2	21.7	20.0
Sm	4.35	4.26	4.28	4.12	4.75	4.37
Eu	1.63	1.39	1.56	1.48	1.63	1.50
Gd	4.92	4.10	4.45	3.95	4.60	4.13
Tb	0.65	0.59	0.69	0.65	0.69	0.64
Dy	3.30	3.30	3.44	3.61	3.55	3.33
Ho	0.64	0.62	0.61	0.66	0.64	0.59
Er	1.71	1.74	1.67	1.66	1.64	1.60
Tm	0.21	0.20	0.20	0.22	0.21	0.21
Yb	1.25	1.24	1.27	1.27	1.22	1.28
Lu	0.17	0.17	0.18	0.16	0.18	0.16
Hf	3.26	3.00	3.21	3.01	3.25	3.60
Ta	1.06	1.05	1.07	1.10	1.02	1.17
Pb	1.55	1.31	1.43	1.88	2.29	1.36
Th	1.89	1.86	1.89	1.96	1.97	1.84
U	0.43	0.40	0.43	0.45	0.44	0.47
	YBYM1601	YBYM1403	YBYM1404	YBYM1410	YBYM1602	YBYM1603
	Picrite	Basalt	Basalt	Basalt	Basalt	Basalt
SiO_2	43.10	46.40	47.70	48.40	48.79	49.47
TiO_2	1.70	2.36	2.34	2.47	2.32	2.31
Al_2O_3	7.62	13.65	13.20	12.25	13.78	13.68
$Fe_2O_3^T$	13.41	12.47	12.36	11.30	11.92	11.90
MnO	0.18	0.15	0.19	0.13	0.15	0.18
MgO	20.30	7.75	7.84	8.36	6.98	6.09
CaO	8.63	10.85	10.20	11.30	8.44	11.55
Na_2O	1.18	2.19	2.68	1.86	3.69	2.14
K_2O	0.39	0.72	0.76	1.02	0.99	0.56
P_2O_5	0.16	0.25	0.22	0.27	0.22	0.20
LOI	3.14	2.07	2.42	2.32	2.67	2.37
Total	99.81	98.86	99.91	99.68	99.95	100.45
Sc	19.1	29.8	29.7	30.7	31.9	31.8
V	290	241	273	311	272	256
Cr	1730	251	336	317	319	309
Co	93.7	51.5	59.4	47.1	45.0	45.0
Ni	1199	83.7	95.0	88.6	99.3	109
Cu	135	59.0	123	135	55.4	112
Zn	105	95.8	88.0	106	118	86.4
Ga	14.5	20.9	20.0	18.7	20.4	21.2
Rb	12.1	11.2	17.5	12.3	42.6	6.64
Sr	202	502	713	495	725	494
Y	15.1	24.4	23.8	22.3	23.9	23.3
Zr	121	184	179	193	177	164

(*continued on next page*)

Table 1 (*continued*)

	YBYM1305	YBYM1406	YBYM1407	YBYM1408	YBYM1411	YBYM1501
	Picrite	Picrite	Picrite	Picrite	Picrite	Picrite
Nb	15.7	24.1	25.1	31.1	27.4	24.5
Cs	0.35	0.23	0.29	1.09	0.32	0.09
Ba	116	347	270	451	234	284
La	14.2	24.6	23.9	31.5	23.5	22.9
Ce	33.0	55.4	55.3	67.5	52.6	50.9
Pr	4.14	7.05	6.85	8.58	6.51	6.24
Nd	18.2	29.2	28.3	36.2	27.8	26.8
Sm	3.90	6.19	6.27	6.82	5.85	5.61
Eu	1.36	2.17	2.08	2.31	2.10	2.04
Gd	3.70	5.93	5.55	5.84	5.60	5.55
Tb	0.56	0.87	0.89	0.91	0.86	0.81
Dy	2.83	4.79	4.40	4.29	4.44	4.43
Ho	0.56	0.92	0.86	0.80	0.88	0.84
Er	1.44	2.46	2.52	2.21	2.37	2.26
Tm	0.18	0.32	0.32	0.28	0.31	0.29
Yb	1.07	2.12	1.96	1.82	1.93	1.81
Lu	0.14	0.28	0.28	0.26	0.26	0.26
Hf	3.16	4.94	4.28	4.87	5.00	4.51
Ta	1.05	1.50	1.60	1.66	1.71	1.61
Pb	1.43	4.85	3.23	4.77	3.44	3.01
Th	1.64	2.49	2.69	3.64	2.63	2.40
U	0.40	0.53	0.58	0.80	0.57	0.51
	YBYM1604	YBYM1401	YBYM1402	YBYM1405	YBYM1409	YBYM1605
	Basalt	Basaltic andesite	Basaltic andesite	Basaltic andesite	Basaltic andesite	Basaltic andesite
SiO_2	48.13	50.70	49.80	51.70	50.90	50.44
TiO_2	2.40	3.40	2.41	2.14	2.37	2.08
Al_2O_3	13.88	12.65	13.70	14.50	12.00	14.71
$Fe_2O_3^T$	11.46	10.99	12.20	10.94	11.42	10.82
MnO	0.17	0.12	0.13	0.14	0.13	0.16
MgO	8.08	6.47	6.56	5.65	7.49	6.40
CaO	8.23	6.96	8.04	7.07	9.97	6.36
Na_2O	3.36	3.15	4.06	3.52	2.08	4.03
K_2O	0.75	2.23	1.00	1.95	1.48	1.43
P_2O_5	0.23	0.38	0.23	0.26	0.29	0.26
LOI	3.04	2.61	2.33	2.01	1.75	3.00
Total	99.73	99.66	100.46	99.88	99.88	99.69
Sc	32.2	24.8	30.9	21.9	29.2	23.1
V	272	270	295	230	287	258
Cr	327	251	246	25.8	491	27.7
Co	46.2	49.0	48.0	45.5	48.6	41.0
Ni	104	72.3	64.1	26.5	187	37.7
Cu	75.4	115	84.4	30.6	106	51.2
Zn	133	101	87.2	89.6	103	111
Ga	20.3	19.2	19.5	20.1	18.7	21.9
Rb	27.1	46.3	36.2	44.9	23.3	29.9
Sr	667	439	736	740	559	611
Y	25.6	26.9	25.6	22.1	24.5	21.4
Zr	186	323	187	211	195	214
Nb	28.6	40.5	25.8	29.8	29.7	31.7
Cs	0.51	0.25	0.26	1.30	1.09	1.29
Ba	201	930	368	785	648	545
La	21.0	48.8	25.4	34.4	32.3	33.2
Ce	50.6	105	57.5	72.0	65.6	71.3
Pr	6.50	12.8	7.15	8.70	8.42	8.39
Nd	28.6	51.1	29.5	35.6	36.4	34.4
Sm	6.13	9.58	6.31	6.41	6.82	6.31
Eu	2.14	2.76	2.13	2.20	2.24	2.22
Gd	5.95	7.72	5.86	5.87	6.12	5.80
Tb	0.90	1.11	0.87	0.83	0.85	0.83
Dy	4.68	5.36	4.85	4.41	4.34	4.15
Ho	0.91	1.00	0.91	0.81	0.80	0.76
Er	2.45	2.71	2.51	2.20	2.22	2.15
Tm	0.32	0.34	0.33	0.29	0.28	0.28
Yb	2.08	2.13	2.03	1.74	1.85	1.73
Lu	0.28	0.28	0.27	0.27	0.25	0.24
Hf	5.14	7.37	4.60	5.36	4.94	5.67
Ta	1.81	2.44	1.62	1.73	1.48	1.98
Pb	3.37	5.79	3.71	6.20	5.26	5.43
Th	2.78	6.26	2.81	4.29	3.36	4.05
U	0.59	1.28	0.55	0.85	0.75	0.89
	BHVO-2[a]	BHVO-2	BHVO-2	BCR-2[a]	BCR-2	BCR-2
	Expected	This study	This study	Expected	This study	This study
SiO_2						

(*continued on next page*)

Table 1 (*continued*)

	YBYM1305	YBYM1406	YBYM1407	YBYM1408	YBYM1411	YBYM1501
	Picrite	Picrite	Picrite	Picrite	Picrite	Picrite
TiO_2						
Al_2O_3						
$Fe_2O_3^T$						
MnO						
MgO						
CaO						
Na_2O						
K_2O						
P_2O_5						
LOI						
Total						
Sc	32	28.6	29.2	33	32.2	31.9
V	317	276	285	416	346	226
Cr	280	255	247	18	19.7	20.0
Co	45	42.6	42.9	37	36.4	36.2
Ni	119	112	113	18	14.5	31.5
Cu	127	121	122	21	27.7	27.0
Zn	103	131	133	127	154	154
Ga	22	20.7	20.9	23	21.3	21.7
Rb	9.11	10.5	10.3	46.9	50.0	49.5
Sr	396	449	441	340	379	379
Y	26	25.3	25.6	37	34.0	34.0
Zr	172	197	196	184	212	213
Nb	18.1	17.8	17.5	12.6	12.2	12.3
Cs	0.1	0.09	0.11	1.1	1.16	1.19
Ba	131	164	162	677	754	776
La	15.2	18.1	17.6	24.9	28.2	28.2
Ce	37.5	45.1	43.4	52.9	59.5	60.0
Pr	5.35	5.85	5.75	6.7	7.35	7.54
Nd	24.5	26.4	25.6	28.7	29.8	29.5
Sm	6.07	6.47	6.92	6.58	6.77	7.01
Eu	2.07	2.36	2.31	1.96	2.12	2.01
Gd	6.24	6.30	6.50	6.75	6.79	6.69
Tb	0.92	1.03	1.02	1.07	1.17	1.13
Dy	5.31	5.34	5.31	6.41	6.30	6.33
Ho	0.98	1.05	1.03	1.28	1.37	1.37
Er	2.54	2.62	2.67	3.66	3.77	3.66
Tm	0.33	0.36	0.32	0.54	0.53	0.58
Yb	2	2.02	1.99	3.38	3.31	3.49
Lu	0.274	0.30	0.28	0.503	0.53	0.55
Hf	4.36	4.76	4.69	4.9	5.00	5.18
Ta	1.14	1.38	1.27	0.74	0.83	0.88
Pb	1.6	1.50	1.59	11	11.0	11.0
Th	1.22	1.28	1.28	5.7	6.00	6.11
U	0.403	0.47	0.46	1.69	1.74	1.76

Notes: oxides in wt%, trace elements in ppm.

[a] Expected data of the BHVO-2, BCR-2 are from http://georem.mpch-mainz.gwdg.de/sample_query_pref.asp

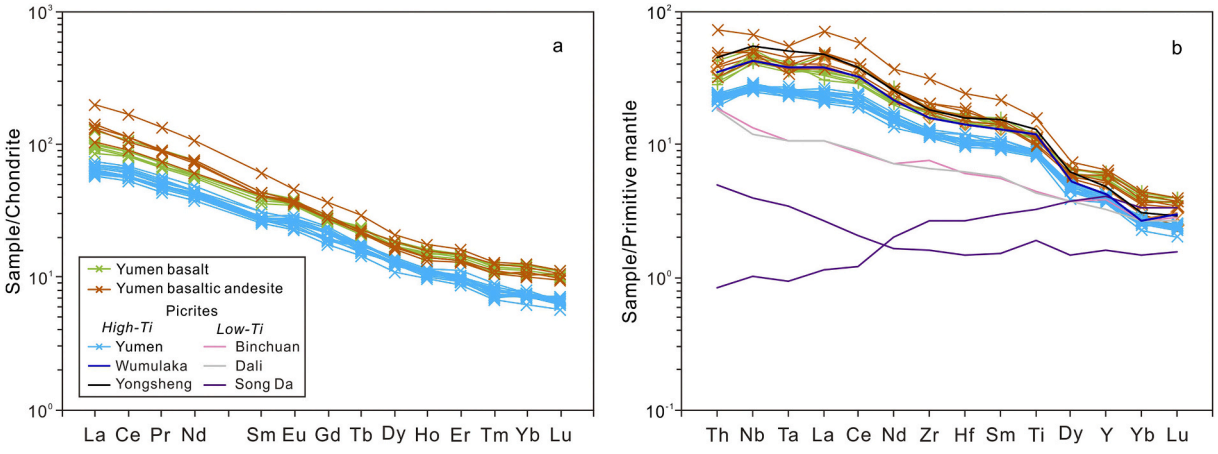

Fig. 3. (a) Chondrite-normalised REE and (b) primitive-mantle-normalised immobile trace element patterns of the Yumen volcanic rocks. The normalising values for chondrite and primitive mantle were taken from Palme and O'Neill (2014). Data sources: Dali (Hanski et al., 2010), Binchuan and Yongsheng (Kamenetsky et al., 2012), Wumulaka (Tao et al., 2015; this study), and Song Da (Li et al., 2012).

Table 2
Whole-rock Sr—Nd isotope data for the Yumen volcanic rocks.

Sample	Rock type	Rb (ppm)	Sr (ppm)	$^{87}Sr/^{86}Sr$ (2σ)	$(^{87}Sr/^{86}Sr)_i$	Sm (ppm)	Nd (ppm)	$^{143}Nd/^{144}Nd$ (2σ)	$(^{143}Nd/^{144}Nd)_i$	$\varepsilon_{Nd}(t)$
YBYM1301	Picrite	14.2	160	0.705045 (11)	0.704095	4.04	19.7	0.512660 (12)	0.512449	2.85
YBYM1303	Picrite	13.3	255	0.705011 (15)	0.704453	4.48	21.3	0.512671 (11)	0.512454	2.95
YBYM1304	Picrite	11.7	240	0.704954 (15)	0.704432	4.17	20.1	0.512659 (10)	0.512445	2.78
YBYM1306	Picrite	10.8	234	0.704834 (14)	0.704340	4.05	19.3	0.512688 (10)	0.512472	3.29
YBYM1307	Picrite	12.1	266	0.704826 (12)	0.704339	4.15	20.1	0.512665 (10)	0.512452	2.91
YBYM1408	Picrite	12.2	314	0.704780 (13)	0.704364	4.12	21.2	0.512672 (8)	0.512472	3.29
YBYM1502	Picrite	13.2	263	0.704828 (14)	0.704291	4.22	19.9	0.512693 (8)	0.512475	3.35
YBYM1403	Basalt	11.2	502	0.705144 (14)	0.704905	6.19	29.2	0.512610 (8)	0.512392	1.73
YBYM1404	Basalt	17.5	713	0.705551 (13)	0.705288	6.27	28.3	0.512620 (9)	0.512392	1.73
YBYM1602	Basalt	42.6	725	0.705980 (15)	0.705351	5.85	27.8	0.512620 (11)	0.512403	1.95
YBYM1603	Basalt	6.64	494	0.705026 (13)	0.704882	5.61	26.8	0.512631 (7)	0.512415	2.18
YBYM1409	Basaltic andesite	23.3	559	0.706307 (11)	0.705861	6.82	36.4	0.512386 (9)	0.512193	−2.15
YBYM1605	Basaltic andesite	29.9	611	0.706260 (11)	0.705736	6.31	34.4	0.512432 (7)	0.512244	−1.16
NBS987	Expected[a]			0.710251(4)						
NBS987	This study			0.710239(13)						
NBS987	This study			0.710260(15)						
NBS987	This study			0.710242(13)						
NBS987	This study			0.710245(12)						
NBS987	This study			0.710242(13)						
JNdi-1	Expected[b]							0.512115 (7)		
JNdi-1	This study							0.512102 (9)		
JNdi-1	This study							0.512119 (9)		
JNdi-1	This study							0.512119 (8)		
JNdi-1	This study							0.512116 (9)		
JNdi-1	This study							0.512116 (7)		
BCR-2	Expected[c]			0.704920				0.512635		
BCR-2	This study			0.705042 (13)				0.512632 (9)		

Chondrite uniform reservoir (CHUR) values ($^{87}Rb/^{86}Sr = 0.0847$, $^{87}Sr/^{86}Sr = 0.7045$; $^{147}Sm/^{144}Nd = 0.1967$, $^{143}Nd/^{144}Nd = 0.512638$) are used for the calculation. $\lambda_{Rb} = 1.42 \times 10^{-11}$ year^{-1} (Steiger and Jäger, 1977); $\lambda_{Sm} = 6.54 \times 10^{-12}$ year^{-1} (Lugmair and Marti, 1978). The $(^{87}Sr/^{86}Sr)_i$, $(^{143}Nd/^{144}Nd)_i$ and $\varepsilon_{Nd}(t)$ of the Yumen volcanic rocks were calculated using age of 260 Ma.

[a] Expected data of the NBS987 is from Miyazaki and Shuto (1998).

[b] Expected data of the JNdi-1 is from Tanaka et al. (2000).

[c] Expected data of the BCR-2 is from http://georem.mpch-mainz.gwdg.de/sample_query_pref.asp

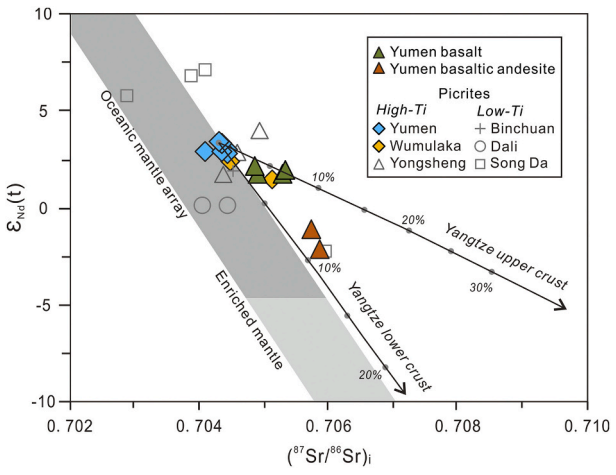

Fig. 4. Plots of initial $\varepsilon_{Nd}(t)$ vs. $(^{87}Sr/^{86}Sr)_i$ for the Yumen volcanic rocks. Data sources for the other picrites are the same as in Fig. 3. The oceanic mantle array is from Zindler and Hart (1986). The parameters of Nd (ppm), ε_{Nd} (260 Ma), Sr (ppm) and $(^{87}Sr/^{86}Sr)_i$ used in the mixing calculation are 20, 3.35, 180 and 0.7043 from Yumen picrites for the mantle-derived magma; 30.7, −38.5, 304, 0.713 and 26.6, −15, 273, 0.715 for the Yangtze lower and upper crust (referred from Bai et al., 2019).

isotopic compositions plot in the oceanic mantle field and have higher ε_{Nd}(260 Ma) and lower $(^{87}Sr/^{86}Sr)_i$ than the Yumen basaltic rocks, and no correlation between ε_{Nd}(260 Ma) and $(^{87}Sr/^{86}Sr)_i$ (Fig. 4). This indicates that the Yumen picrites have not experienced obvious crustal contamination. However, ε_{Nd}(260 Ma) values of the Yumen basaltic rocks exhibit a negative correlation with $(^{87}Sr/^{86}Sr)_i$, indicating crustal contamination (Fig. 4), because continental crust has higher $(^{87}Sr/^{86}Sr)_i$ values than the mantle (Rudnick and Gao, 2014). In the mixing modelling of Sr—Nd isotopes, because of the primitively compositional features, the average Sr and Nd concentrations of the Yumen picrites and the Sr—Nd isotope values of the most depleted picrite sample are used as the composition of primitive magma end-member [Sm: 20 ppm, ε_{Nd}(260 Ma): 3.35, Sr: 180 ppm, $(^{87}Sr/^{86}Sr)_i$: 0.7043]. The compositions of Yangtze lower and upper crust in which our samples outcrop are regard as the enriched end-member [Sm: 30.7 ppm, ε_{Nd}(260 Ma): −38.5, Sr: 304 ppm, $(^{87}Sr/^{86}Sr)_i$: 0.713 for Yangtze lower crust; Sm: 26.6 ppm, ε_{Nd}(260 Ma): −15, Sr: 273 ppm, $(^{87}Sr/^{86}Sr)_i$: 0.715 for Yangtze upper crust; Bai et al., 2019]. The Sr—Nd isotopic compositions of the Yumen basaltic rocks can be explained by the less than 10% contamination of Yangtze crustal component. Crustal contamination can also account for the negative Nb—Ta anomalies of the Yumen basaltic rocks (Fig. 3b). The content of MgO from 8 wt% decrease to 5 wt%, whole-rock CaO contents of the Yumen basaltic samples decrease, but Al_2O_3 contents increase (Fig. S3). There is also no Eu depletion (Fig. 3a). These observations suggest that clinopyroxene started to crystallise at 8 wt% MgO, and that plagioclase crystallisation did not occur at MgO > 5 wt%. The low whole-rock Ni contents in the basaltic rocks are due to fractional crystallisation of olivine (Fig. S3f). These fractionations are consistent with the presence of clinopyroxene and olivine in the Yumen picrites-basalts and plagioclase phenocrysts in basaltic rocks (Fig. S1c–d). The Yumen picritic-basaltic lavas occur between overlying Lower Triassic sediments and underlying Permian limestones and have an interbedded contact relationship between them (Fig. 1), indicating these picrites and basaltic rocks and ELIP are of the same age. Therefore, we suggest that the Yumen picritic-basaltic lavas are part of the ELIP high-Ti group, and were produced by variable assimilation–fractional crystallisation (AFC) of the ELIP high-Ti magmas.

Table 3
Whole-rock chalcophile element data for the Yumen volcanic rocks.

Sample	Rock type	Ni (ppm)	Ir (ppb)	Ru (ppb)	Rh (ppb)	Pt (ppb)	Pd (ppb)	Cu (ppm)
YBYM1301	Picrite	868	0.61	2.74	0.76	11.4	6.58	127
YBYM1302	Picrite	851	0.61	2.85	0.89	13.2	6.38	128
YBYM1303	Picrite	863	0.56	3.08	0.82	11.9	6.57	145
YBYM1304	Picrite	846	0.90	2.80	0.79	11.9	5.35	129
YBYM1305	Picrite	831	0.67	2.82	0.75	12.2	5.28	81.9
YBYM1306	Picrite	849	0.59	2.88	0.75	11.8	5.39	121
YBYM1307	Picrite	835	0.57	2.69	0.72	10.4	4.95	100
YBYM1406	Picrite	591	0.57	2.65	0.68	9.95	4.32	67.2
YBYM1412	Picrite	829	0.60	2.74	0.67	11.3	5.37	138
YBYM1502	Picrite	864	0.50	2.82	0.72	11.2	5.79	137
YBYM1403	Basalt	83.7	0.04	0.05	0.02	0.30	0.60	59.0
YBYM1404	Basalt	95.0	0.22	0.13	0.26	6.17	2.84	123
YBYM1602	Basalt	99.3	0.13	0.09	0.30	7.90	3.52	55.4
YBYM1603	Basalt	109	0.11	0.09	0.31	6.02	3.65	112
YBYM1604	Basalt	104	0.15	0.09	0.28	7.29	3.79	75.4
YBYM1401	Basaltic andesite	72.3	0.08	0.17	0.25	4.79	3.68	115
YBYM1402	Basaltic andesite	64.1	0.11	0.09	0.01	0.34	0.18	84.4
YBYM1405	Basaltic andesite	26.5	0.02	0.05	0.01	0.14	0.30	30.6
YBYM1405[a]			0.01	0.04	0.01	0.14	0.39	
YBYM1605	Basaltic andesite	37.7	0.03	0.03	0.01	0.11	0.36	51.2
WGB-1	Expected[b]		0.27 ± 0.03	0.15 ± 0.02	0.18 ± 0.02	4.95 ± 0.52	11.8 ± 0.8	
	This study		0.26	0.21	0.17	4.42	14.6	

[a] Duplicate samples.
[b] Expected data of the WGB-1 are from Qi et al., 2011

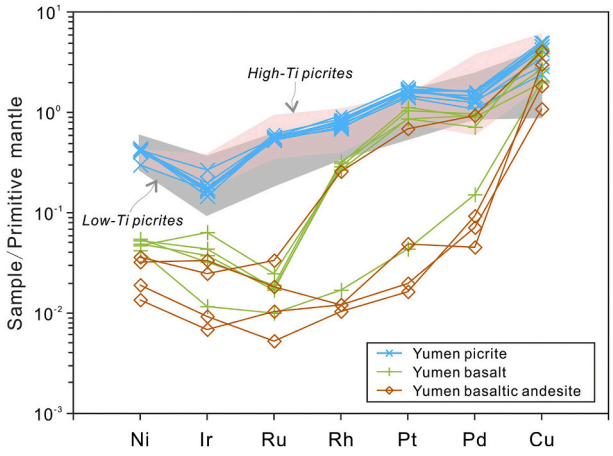

Fig. 5. Primitive-mantle-normalised Ni–PGE–Cu patterns for the Yumen volcanic rocks. Data sources for the fields of ELIP high- and low-Ti picrites are the same as in Fig. 3. The normalising values for primitive mantle were taken from Palme and O'Neill (2014).

5.2. Peridotitic mantle source for high-Ti basalts in the ELIP

There are two contrasting views regarding the lithology of the mantle source of the ELIP high-Ti basalts (i.e., peridotite vs. pyroxenite; e.g., Kamenetsky et al., 2012; Ren et al., 2017; Yao et al., 2019). To address this issue, primary magma compositions were calculated by adding/subtracting equilibrium olivine to the compositions of olivine-hosted melt inclusions (MgO > 8 wt%; Hanski et al., 2010; Kamenetsky et al., 2012) until the melt is in equilibrium with Fo93 olivine, using a $K_d^{Fe/Mg}$ (olivine/melt) of 0.30 (Roeder and Emslie, 1970) and assumed Fe^{2+}/Fe^T ratio of 0.90 for the melt. Whole-rock MgO/FeO ratios of the Yumen picrites are in equilibrium with Fo92 olivine, meaning that the whole-rock compositions of the Yumen picrites approximate primary magma compositions. The MgO, SiO_2, Al_2O_3, and CaO contents of the Yumen picrites and ELIP high-Ti primitive magmas plot in the field of experimental melts of garnet peridotite (Fig. 6a–d). In addition to the involvement of recycled oceanic mafic crust, Zhang et al. (2019) proposed that high-pressure melting in the mantle source of the ELIP high-Ti basalts could also explain their slightly higher TiO_2 contents than low-Ti basalts, because Ti in garnet is incompatible and the proportion of garnet in the mantle source increases with depth. Yang and Zhou (2013) proposed that the FC3MS parameter ($FeO/CaO - 3 \times MgO/SiO_2$, all in wt%), which is unaffected by pressure–temperature, is a better indicator for distinguishing pyroxenite- and peridotite-derived melts, because modelling calculations show that FC3MS values of pyroxenite melts (>0.65) are higher than those of peridotite melts (<0.65). Calculated FC3MS values of the Yumen picrites and primitive magmas of the ELIP both plot in the peridotite-derived melt field (Fig. 6e). Based on the lower bulk partition coefficient for Zn and lower $K_D^{Zn/Fe}$ in eclogite/pyroxenite relative to peridotite, Le Roux et al. (2010) proposed that melts derived from eclogite/pyroxenite should have higher 10000Zn/Fe (>14) ratios than peridotite-derived melts (6–12.5). The 10000Zn/Fe ratios of the ELIP picrites plot in the field of peridotite-derived melts (Fig. 6f). Therefore, these whole-rock geochemical features, along with the depleted Sr—Nd isotopic compositions ($\varepsilon_{Nd}(t) = +1.4$ to $+4.0$; $(^{87}Sr/^{86}Sr)_i = 0.70410$ to 0.70515), indicate that the ELIP high-Ti basalts were derived from a depleted mantle source consisting of garnet peridotite.

5.3. Effects of source physicochemical melting conditions on olivine chemistry

In contrast to the high-Ni and low-Mn feature of olivine phenocrysts, the compositions of ELIP high-Ti primitive magmas calculated from olivine-hosted melt inclusions and whole-rock FC3MS and Zn/Fe values for the ELIP picrites are similar to peridotite-derived melts (Fig. 6). Yao et al. (2019) noted that the high Mn/Zn and low Zn/Fe ratios of olivine phenocrysts with Fo > 85 in the ELIP picrites were similar to those from peridotite-derived melts. Recent experimental studies (Matzen et al., 2013, 2017) have shown that the partition coefficients of Ni and Mn in olivine are mainly controlled by the source melting *P–T* conditions and MgO contents of the equilibrium melts, respectively. As such, Mg-rich melts derived from mantle peridotite at high *P–T* conditions can produce high-Ni and low-Mn olivine during low-pressure crystallisation. Hence, we estimated the effect of different *P–T* conditions on the composition of olivine phenocrysts in the ELIP.

Using the Al concentrations of primary olivine–Cr-spinel, the Al-in-olivine thermometer of Coogan et al. (2014) was used to estimate the

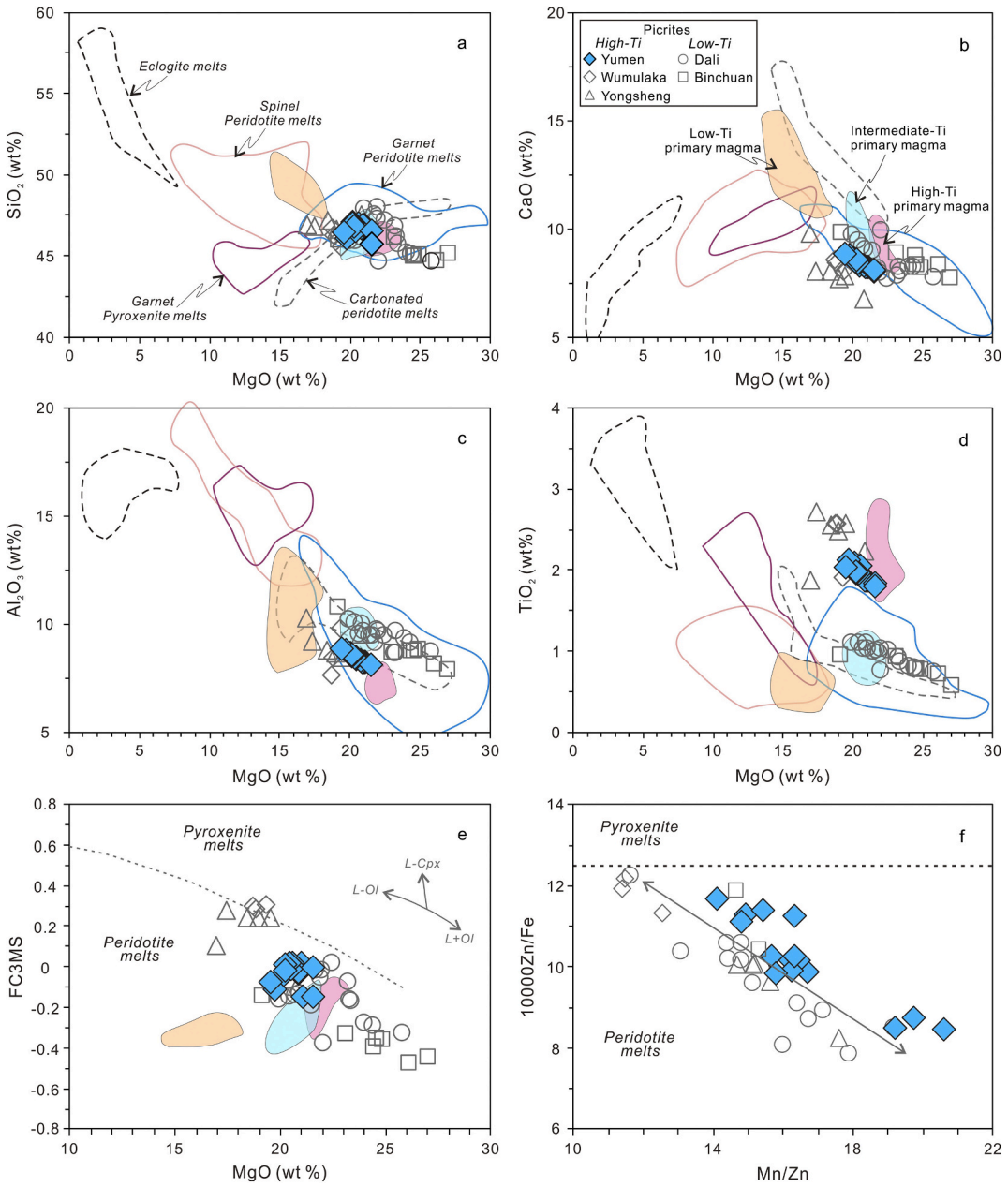

Fig. 6. Comparison of the Yumen picrites and primitive magmas with experimentally derived melts. MgO vs. (a) SiO_2, (b) CaO, (c) Al_2O_3, (d) TiO_2, and (e) FC3MS. The line separating peridotite- and pyroxenite-derived melts is from Yang and Zhou (2013). (f) Mn/Zn vs. 10000Zn/Fe. The lines separating peridotite- and pyroxenite-derived melts are from Le Roux et al. (2010). Data sources for the other picrites are the same as in Fig. 3. Melt sources: eclogite (Kogiso and Hirschmann, 2006; Pertermann and Hirschmann, 2003), garnet pyroxenite (Hirschmann et al., 2003; Keshav et al., 2004; Kogiso et al., 2003), spinel peridotite (Hirose and Kushiro, 1993), garnet peridotite (Walter, 1998), and carbonated peridotite (3 GPa and 2.5 wt% CO_2; Dasgupta et al., 2007).

crystallisation temperatures of primary olivines (Fo > 86) in the Yumen high-Ti picrites. The crystallisation temperatures of olivine in the high-Ti magmas (1410–1550 °C; Fig. 7a) are higher than those of the low-Ti magmas (1250–1360 °C; Xu and Liu, 2016). Using the method of Lee et al. (2009), the *P–T* conditions of mantle melting for the primitive high- and low-Ti magmas in the ELIP can be calculated from their primitive melt compositions. Given that the ELIP might have been derived from hydrous mantle (Liu et al., 2017; Xu et al., 2020), the water contents of the ELIP primitive magmas were estimated from their Ce contents and the H_2O/Ce ratio (~200) of least-degassed OIBs (Dixon et al., 2002). The Ce contents of the primary high- and low-Ti magmas can be calculated from the olivine-hosted melt inclusion data of Kamenetsky et al. (2012) using the equation $Ce_{primitive\ magma} = Ce_{melt\ inclusion} \times (1 - X)$, where X is the proportion of added olivine. The estimated water contents of the Yumen picrites and high- and low-Ti primitive magmas are 0.8, 1.3, and 0.25 wt%, respectively, which are similar to OIBs (0.2–1.6 wt% H_2O; Herzberg and Asimow, 2008). Although these estimated water contents have considerable uncertainty, it does not significantly affect the following discussion.

The ELIP high-Ti magmas were derived from mantle peridotite at higher mantle potential *P–T* conditions (4.0–5.4 GPa and 1620–1660 °C) than MORBs (~1 GPa and ~ 1350 °C) and the ELIP low-Ti magmas (1.5–3.0 GPa and 1410–1530 °C; Fig. 7b). Here our estimated mantle potential temperatures for the ELIP low-Ti magma are consistent with those calculated by primary melt composition of the ELIP low-Ti basalts (~1400 to ~1550 °C; Shellnutt and Pham, 2018). Based on experimental results for the temperature effect on Ni partition coefficients in olivine, every 100 °C increase in the source melting temperature can

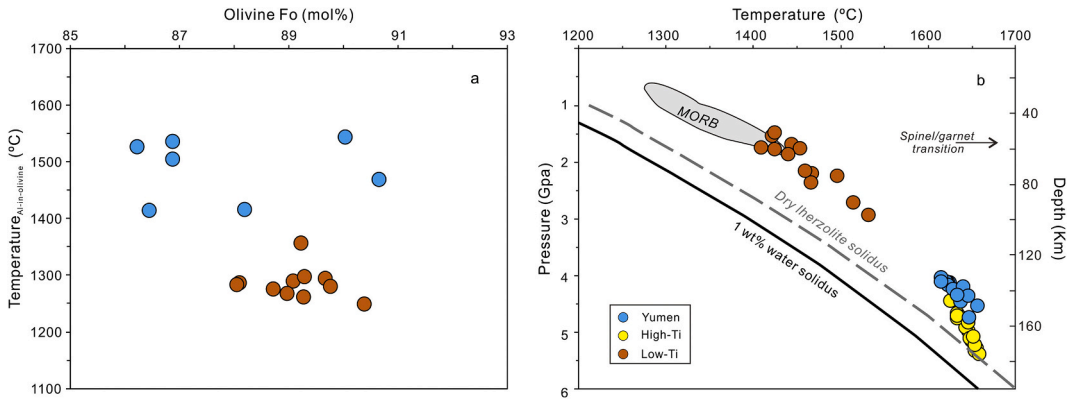

Fig. 7. (a) Olivine crystallisation temperatures of the Yumen picrites obtained by Al-in-olivine thermometry. The crystallisation temperatures for olivine in the ELIP low-Ti magmas are from Xu and Liu (2016). (b) Pressure–temperature conditions of source melting for the Yumen picrites and ELIP low- and high-Ti magmas. The method used and MORB field are from Lee et al. (2009). The solidus of dry and 1 wt% water lherzolite were taken from Katz et al. (2003).

result in a decrease of ~455 ppm Ni in olivine (Matzen et al., 2013). The difference in the source melting temperatures between the Yumen picrites and MORBs is ~250 °C. Thus, we can correct for the effect of melting temperature on the Ni content in olivine in the Yumen picrites using the equation: $Ni_{corrected} = Ni_{olivine} - 2.5 \times 455$. In a Fo–Ni plot, the corrected olivine data for the Yumen picrites plot in the field for olivine from MORBs (Fig. 8a). The partition coefficient for Mn between olivine–melt depends mainly on the melt MgO content and increases from 0.65 at 22 wt% MgO (i.e., a high-Ti primitive magma) to 0.8 at 16 wt% MgO (i.e., a low-Ti primitive magma; Matzen et al., 2017). The effect of the melt MgO content on the olivine Mn content in the Yumen picrites was corrected using the equation: $Mn_{corrected} = 0.8/0.65 \times Mn_{olivine}$. The corrected olivine Mn contents are similar to those of olivines in the ELIP low-Ti magmas and MORBs (Fig. 8b). These lines of evidence do not completely rule out a contribution from a pyroxenitic component to the ELIP, but demonstrate that variations in the physicochemical melting conditions can explain the different olivine Ni and Mn contents in the ELIP high- and low-Ti picrites and basalts.

5.4. PGE constraints on magma evolution in the ELIP

5.4.1. PGE partitioning

The partition coefficients for PGEs in sulfide liquids range up to 10^5, and thus deviations from the trend lines in plots of $Mg^{\#}$–PGEs (Fig. 9) for the basaltic samples indicate magmatic sulfide segregation. However, PGE partitioning in basaltic magmas is not fully understood. Based on negative correlations between whole-rock $(Pt/Ru)_N$ and $(Rh/Ru)_N$ vs. $Mg^{\#}$ ($Mg/[Mg + Fe^T]$) and the approximately constant $(Pt/Rh)_N$, Li et al. (2016) suggested that Pt and Rh behaved incompatibly during magma differentiation in the ELIP. However, correlations between whole-rock $Mg^{\#}$ values and PGE contents may be a better way to investigate the PGE fractionations in the ELIP. Whole-rock PPGE (Pd, Pt, and Rh) contents of the ELIP Pd-undepleted samples show no obvious variations, whereas the IPGE (Ru and Ir) contents decrease significantly with decreasing whole-rock $Mg^{\#}$ values (Fig. 9a–e), indicating that the partition coefficients were close to one for Pd, Pt, and Rh, and that Ir and Ru were compatible. The obvious positive correlation between whole-rock Cr and Ru contents at Cr > 300 ppm (Fig. 9f) implies that Ru (Ir) is compatible in Cr-spinel, which is consistent with previous studies (e.g., Arguin et al., 2016; Park et al., 2012; Righter et al., 2004). Rhodium exhibits intermediate behaviour and its partition coefficient is influenced by temperature and the oxidation state (Arguin et al., 2016; Brenan et al., 2003, 2012). We also propose that Pd and Pt could have such an intermediate behaviour in basaltic magma, but the reasons for this are unclear.

5.4.2. Cause of magmatic sulfide saturation

Due to the extremely high partition coefficients for PGEs in sulfide liquid relative to Ni, Cu, and lithophile elements (e.g., Yb), the ratio between these elements is highly sensitive to sulfide segregation. Given the possible addition of Cu during post-magmatic hydrothermal alteration, Li et al. (2016) proposed that 10,000 × Pd/Yb values of >100 can be used to infer Pd depletion and magmatic sulfide saturation and segregation. We used correlations between whole-rock 10,000 × Pd/Yb and $Mg^{\#}$, $(Th/Nb)_N$, and $\varepsilon_{Nd}(t)$ values to examine the factors responsible for sulfide saturation of the ELIP basaltic rocks (Fig. 10). No systematic

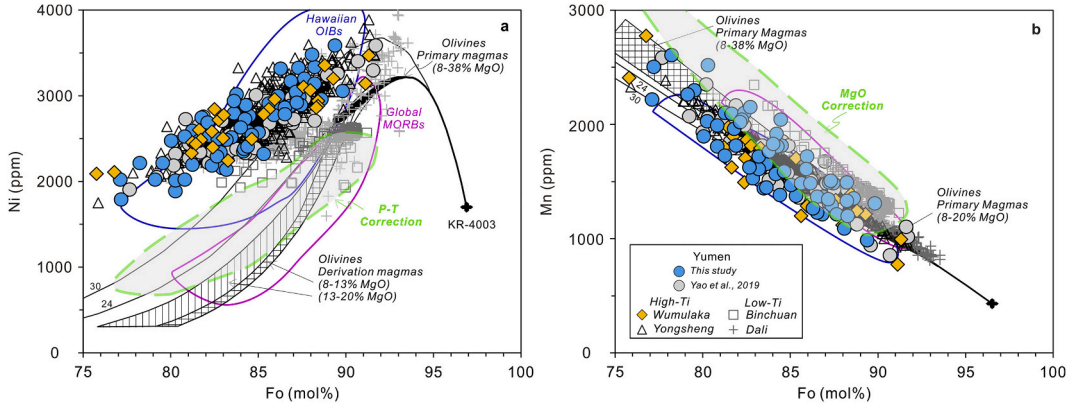

Fig. 8. Corrected Ni and Mn contents in olivine from the Yumen picrites, which accounts for the source melting conditions. Data sources: Dali (Hanski et al., 2010), Binchuan and Yongsheng (Kamenetsky et al., 2012), Wumulaka (this study), and Song Da (Li et al., 2016).

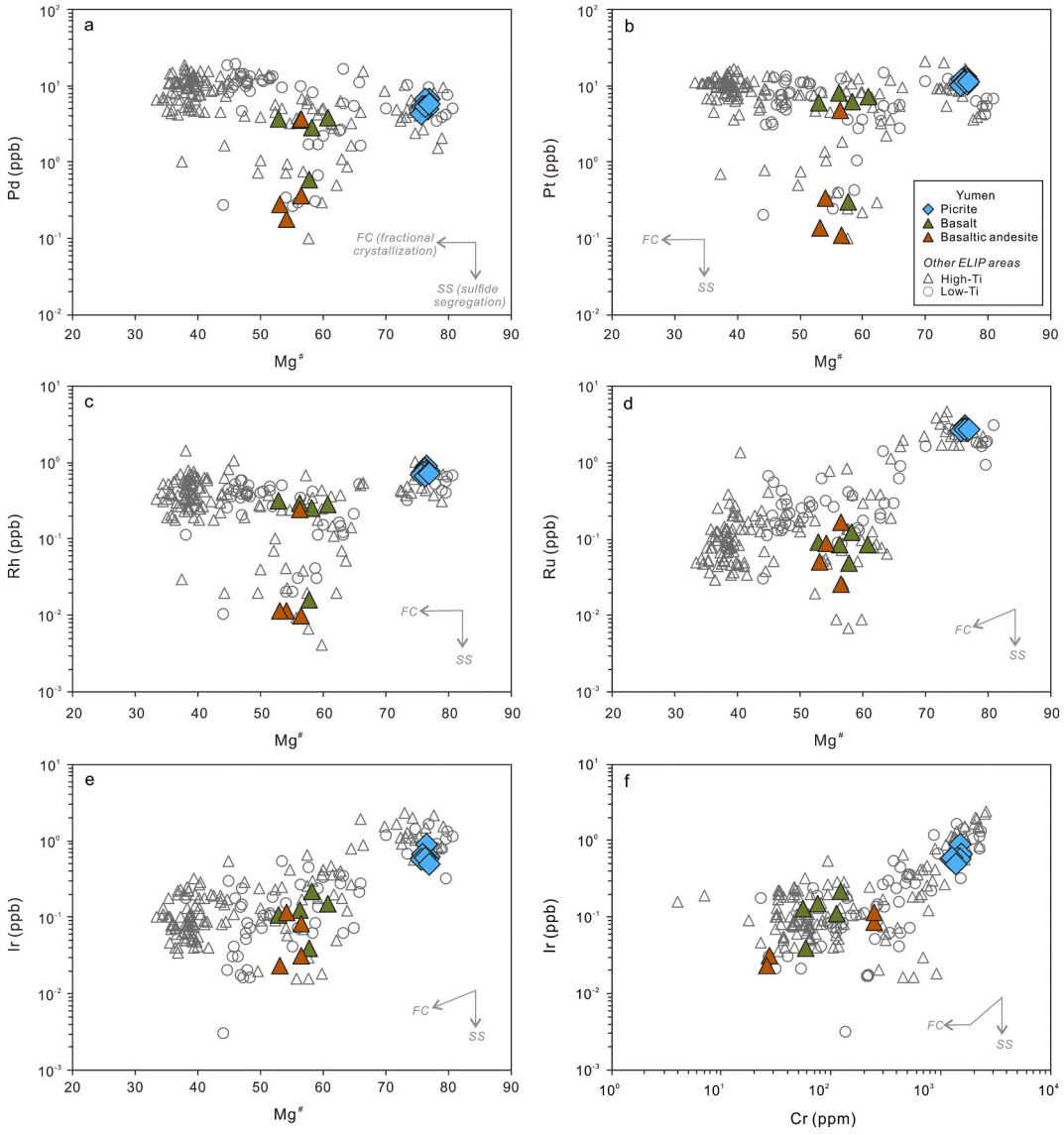

Fig. 9. Plots of whole-rock $Mg^{\#}$ values (100 × Mg/[Mg + Fe^{T}]) vs. (a) Pd, (b) Pt, (c) Ru, (d) Rh, and (e) Ir, and (f) Cr vs. Ir, for the Yumen volcanic rocks. Data sources for the other ELIP samples are listed in Table S3.

PGE differences characterise the ELIP high- and low-Ti samples, and all the Pd-depleted samples are basaltic rocks. Similar to other ELIP basalts, the range of whole-rock $Mg^{\#}$ values of the Pd-depleted samples is similar to that of the Pd-undepleted Yumen basalt samples, indicating that fractional crystallisation was not the main cause of magmatic sulfide saturation in the ELIP (Fig. 10a). Furthermore, although the Pd-depleted Yumen basalt samples have relatively low $\varepsilon_{Nd}(t)$, there is no difference in $(Th/Nb)_N$ between the Pd-depleted and -undepleted samples (Fig. 10b–c). This suggests that selective assimilation of crustal sulfide, rather than crustal silicate component, was the probable cause of sulfide saturation in the ELIP basaltic rocks. Sulfide saturation and segregation in basaltic magmas is key for the formation of magmatic Cu–Ni–PGE sulfide deposits in LIPs. Zhou et al. (2008) suggested that, in the ELIP, the high-Ti magma was associated with the formation of giant Fe–Ti–V oxide ore deposits (e.g., Panzhihua and Baima), whereas the low-Ti magma was associated with the formation of Cu–Ni–PGE sulfide deposits (e.g., Jinbaoshan, Limahe, and Zhubu; Fig. 1b). However, Zhang et al. (2017) investigated the parental magmas of the mafic–ultramafic intrusions hosting magmatic Cu–Ni–PGE sulfide deposits in the ELIP, including those at Nantianwan (1.03 wt% TiO_2 and 15.06 wt% MgO), Yangliuping (1.8 wt% TiO_2 and 10.08 wt% MgO), and Limahe (1.89 wt % TiO_2 and 16.67 wt% MgO), and showed that these range from low- to high-Ti compositions. The high-Ti magma may have been more likely to produce Fe–Ti–V oxide ore deposits due to its high Ti and Fe concentrations (Zhou et al., 2008) or more oxidised mantle source (Bai et al., 2019). However, the present study shows that the ELIP high-Ti magma also had the potential to form magmatic Cu–Ni–PGE sulfide deposits. Therefore, mafic–ultramafic rocks derived from high-Ti magmas should be targets for global Ni exploration in LIPs.

5.5. *A petrogenetic model for the ELIP high-Ti picrites and basaltic rocks*

Based on previously reported data for the ELIP and our new data for the Yumen picritic-basaltic samples, we suggest that the ELIP high-Ti magmas were generated by partial melting of a depleted, deep, garnet peridotite source, and then experienced variable fractional crystallisation and crustal contamination by different crustal components (e.g., silicates and sulfides), and sulfide liquid segregation. The petrogenetic model we propose for the ELIP high-Ti picrites and basaltic rocks involves: (1) ascent of the anomalously hot Emeishan mantle plume above the garnet peridotite solidus and melting at depths of ~140–160 km, which produced the Mg–Ti–Ni-rich primary magmas; (2) rapid ascent of

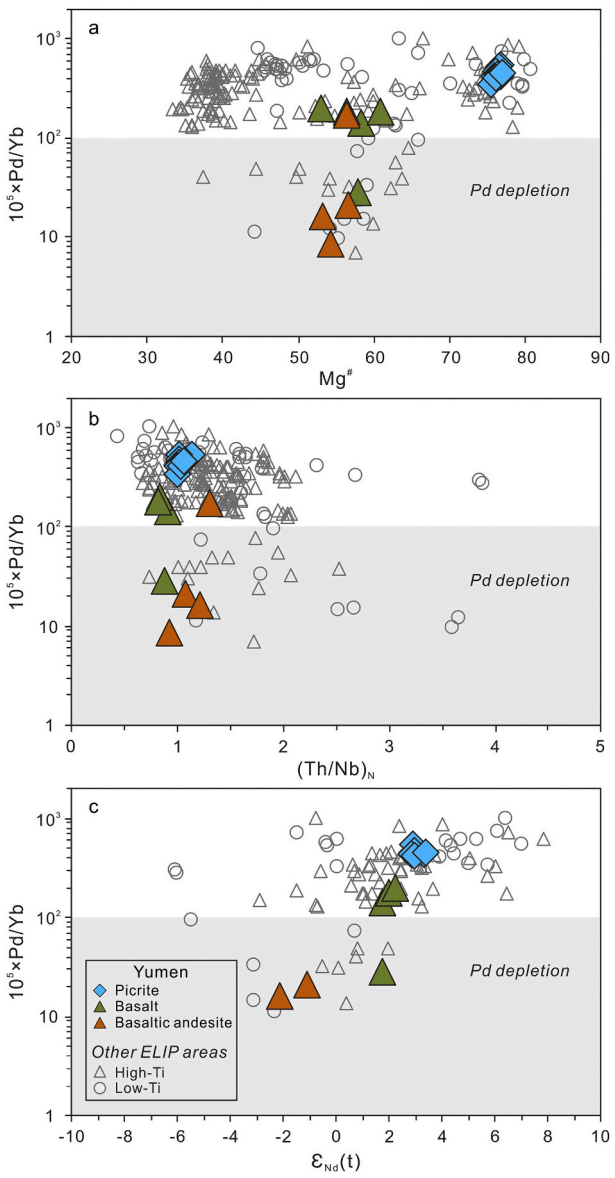

Fig. 10. Plots of whole-rock 10,000 × Pd/Yb vs. $Mg^{\#}$ values (100 × Mg/[Mg + Fe]), $\varepsilon_{Nd}(t)$, and $(Th/Nb)_N$ for the Yumen volcanic rocks. The Pd depletion boundary was taken from Li et al. (2016). Data are from this study and sources listed in Table S3. The normalising values for primitive mantle (Th and Nb) were taken from Palme and O'Neill (2014).

some primitive magmas to the surface, which experienced little fractional crystallisation of Cr-spinel and high-Ni and low-Mn olivine, thereby forming the ELIP high-Ti picrites; and (3) slow ascent of some primitive magmas to the surface, which experienced large amounts of fractional crystallisation and variable degrees of crustal contamination, thereby forming the ELIP high-Ti basaltic rocks. The variable degrees of fractional crystallisation and crustal contamination resulted in the formation of four types of ELIP high-Ti basaltic rocks: (1) high ε_{Nd} (>0) and Pd-undepleted (only experienced fractional crystallisation); (2) low ε_{Nd} (<0) and Pd-undepleted (experienced fractional crystallisation and contamination by a crustal silicate component); (3) high ε_{Nd} and Pd-depleted (experienced fractional crystallisation and contamination by a crustal sulfide component); and (4) low ε_{Nd} and Pd-depleted (experienced fractional crystallisation and contamination by crustal silicate and sulfide components). Mafic–ultramafic intrusions formed at shallow crustal levels from Pd-depleted basaltic rocks have the potential to host magmatic Cu–Ni–PGE sulfide deposits.

Therefore, multiple garnet peridotite-derived magmas with different compositions were involved in the formation of the Yumen picrites and basaltic rocks, and interactions with the continental lithosphere were also significant. More importantly, this study shows that polybaric melting in a LIP can cause differences in olivine trace element contents, which were previously regarded to reflect different mantle source lithologies (i.e., peridotite vs. pyroxenite). This implies that olivine trace element contents should be used with caution when distinguishing peridotite- and pyroxenite-derived melts, and that contributions by pyroxenitic component may have been overestimated in other LIPs.

6. Conclusions

We present mineral compositional and whole-rock major and trace element, Sr—Nd isotope, and PGE concentration data for ELIP high-Ti picritic-basaltic samples from Yumen. These data and a compilation of previously published data for the ELIP allow us to draw the following conclusions:

(1) The Yumen picritic-basaltic lavas have the same stratigraphy as the ELIP, and similar whole-rock and mineral compositions to the ELIP high-Ti picrites, which indicate they are part of the ELIP high-Ti group.
(2) The compositions and FC3SM values of the primitive magmas, and 10000Zn/Fe values and Sr—Nd isotopic compositions of the ELIP high-Ti picrites indicate derivation from depleted garnet peridotite.
(3) Differences in olivine Ni and Mn contents in the ELIP high- and low-Ti picrites can be explained by variations in the physico-chemical source melting conditions rather than the nature of the mantle source lithology.
(4) Correlations between whole-rock $Mg^{\#}$ values and PGE contents indicate that Ru and Ir behaved compatibly, and Pd, Pt, and Rh had partition coefficients of close to one in the ELIP basaltic magma system.
(5) No correlations were observed between whole-rock 10,000 × Pd/Yb and $Mg^{\#}$, $(Th/Nb)_N$, and $\varepsilon_{Nd}(t)$ values, which indicate addition of crustal sulfur caused magmatic sulfide saturation in the ELIP. Variable degrees of fractional crystallisation and crustal contamination involving silicate and/or sulfide components by the high-Ti magmas resulted in the formation of different high-Ti basaltic rocks in the ELIP.

Supplementary data to this article can be found online at https://doi.org/10.1016/j.lithos.2021.106364.

Declaration of Competing Interest

The authors declare that they have no known competing financial interests or personal relationships that could have appeared to influence the work reported in this paper.

Acknowledgments

This work is supported by the Strategic Priority Research Program of the Chinese Academy of Sciences (Grant No.XDB18030204), the National Science Foundation of China (Grants 41425011, 41572074, and 41273049), and Natural Science Foundation of Shandong Province (No. ZR2020MD070). We thank Yan Tao for providing Wumulaka picrite samples, Minwu Liu for their assistances in EMPA, Jing Hu and Yan Huang for trace element analyses by ICP-MS, Liang Qi and Yifan Yin for PGE concentrations analyses by ICP–MS, Leilei Dong and Chaofeng Li for Sr—Nd isotope analyses by Nu Plasma. Constructive reviews by the anonymous reviewers and useful guidance from the editor are greatly appreciated.

References

Ali, J.R., Thompson, G.M., Zhou, M.-F., Song, X.Y., 2005. Emeishan large igneous province, SW China. Lithos 79, 475–489.

Anh, T.V., Pang, K.-N., Chung, S.-L., Lin, H.-M., Hoa, T.T., Anh, T.T., Yang, H.-J., 2011. The Song Da magmatic suite revisited: a petrologic, geochemical and Sr–Nd isotopic study on picrites, flood basalts and silicate volcanic rocks. J. Asian Earth Sci. 42, 1341–1355.

Arguin, J.-P., Pagé, P., Barnes, S.-J., Yu, S.-Y., Song, X.-Y., 2016. The effect of chromite crystallization on the distribution of osmium, iridium, ruthenium and rhodium in picritic magmas: an example from the Emeishan Large Igneous Province, Southwestern China. J. Petrol. 57, 1019–1048.

Bai, Z., Zhong, H., Hu, R., Zhu, W., Hu, W., 2019. Composition of the chilled marginal rocks of the Panzhihua Layered Intrusion, Emeishan Large Igneous Province, SW China: implications for Parental Magma compositions, sulfide saturation history and Fe–Ti oxide mineralization. J. Petrol. 60, 619–648.

Brenan, J., McDonough, W., Dalpe, C., 2003. Experimental constraints on the partitioning of rhenium and some platinum-group elements between olivine and silicate melt. Earth Planet. Sci. Lett. 212, 135–150.

Brenan, J.M., Finnigan, C.F., McDonough, W.F., Homolova, V., 2012. Experimental constraints on the partitioning of Ru, Rh, Ir, Pt and Pd between chromite and silicate melt: the importance of ferric iron. Chem. Geol. 302, 16–32.

Cawood, P.A., Wang, Y., Xu, Y., Zhao, G., 2013. Locating South China in Rodinia and Gondwana: a fragment of greater India lithosphere? Geology 41, 903–906.

Chung, S.-L., Jahn, B.-M., 1995. Plume-lithosphere interaction in generation of the Emeishan flood basalts at the Permian-Triassic boundary. Geology 23, 889–892.

Coogan, L., Saunders, A., Wilson, R., 2014. Aluminum-in-olivine thermometry of primitive basalts: evidence of an anomalously hot mantle source for large igneous provinces. Chem. Geol. 368, 1–10.

Dasgupta, R., Hirschmann, M.M., Smith, N.D., 2007. Partial melting experiments of peridotite + CO_2 at 3 GPa and genesis of alkalic ocean island basalts. J. Petrol. 48, 2093–2124.

Dixon, J.E., Leist, L., Langmuir, C., Schilling, J.G., 2002. Recycled dehydrated lithosphereobserved in plume-influenced mid-ocean-ridge basalt. Nature 420, 385–389.

Ellam, R.M., 2006. New constraints on the petrogenesis of the Nuanetsi picrite basalts from Pb and Hf isotope data. Earth Planet. Sci. Lett. 245, 153–161.

Gavrilenko, M., Herzberg, C., Vidito, C., Carr, M.J., Tenner, T., Ozerov, A., 2016. A calcium-in-olivine geohygrometer and its application to subduction zone magmatism. J. Petrol. 57, 1811–1832.

Hanski, E., Kamenetsky, V.S., Luo, Z.-Y., Xu, Y.-G., Kuzmin, D.V., 2010. Primitive magmas in the Emeishan large igneous province, southwestern China and northern Vietnam. Lithos 119, 75–90.

He, B., Xu, Y.-G., Chung, S.-L., Xiao, L., Wang, Y., 2003. Sedimentary evidence for a rapid, kilometer-scale crustal doming prior to the eruption of the Emeishan flood basalts. Earth Planet. Sci. Lett. 213, 391–405.

Heinonen, J.S., Fusswinkel, T., 2017. High Ni and low Mn/Fe in olivine phenocrysts of the Karoo meimechites do not reflect pyroxenitic mantle sources. Chem. Geol. 467, 131–142.

Herzberg, C., 2011. Identification of Source Lithology in the Hawaiian and Canary Islands: implications for Origins. J. Petrol. 52, 113–146.

Herzberg, C., Asimow, P.D., 2008. Petrology of some oceanic island basalts: PRIMELT2. XLS software for primary magma calculation. Geochem. Geophys. Geosyst. 9, Q09001.

Hirose, K., Kushiro, I., 1993. Partial melting of dry peridotites at high pressures: determination of compositions of melts segregated from peridotite using aggregates of diamond. Earth Planet. Sci. Lett. 114, 477–489.

Hirschmann, M.M., Kogiso, T., Baker, M.B., Stolper, E.M., 2003. Alkalic magmas generated by partial melting of garnet pyroxenite. Geology 31, 481–484.

Hole, M.J., 2018. Mineralogical and geochemical evidence for polybaric fractional crystallization of continental flood basalts and implications for identification of peridotite and pyroxenite source lithologies. Earth Sci. Rev. 176, 51–67.

Howarth, G.H., Harris, C., 2017. Discriminating between pyroxenite and peridotite sources for continental flood basalts (CFB) in southern Africa using olivine chemistry. Earth Planet. Sci. Lett. 475, 143–151.

Kamenetsky, V.S., Chung, S.-L., Kamenetsky, M.B., Kuzmin, D.V., 2012. Picrites from the Emeishan Large Igneous Province, SW China: a compositional continuum in primitive magmas and their respective mantle sources. J. Petrol. 53, 2095–2113.

Katz, R.F., Spiegelman, M., Langmuir, C.H., 2003. A new parameterization of hydrous mantle melting. Geochem. Geophy. Geosy. 4, 1073.

Keshav, S., Gudfinnsson, G.H., Sen, G., Fei, Y., 2004. High-pressure melting experiments on garnet clinopyroxenite and the alkalic to tholeiitic transition in ocean-island basalts. Earth Planet. Sci. Lett. 223, 365–379.

Kogiso, T., Hirschmann, M.M., 2006. Partial melting experiments of bimineralic eclogite and the role of recycled mafic oceanic crust in the genesis of ocean island basalts. Earth Planet. Sci. Lett. 249, 188–199.

Kogiso, T., Hirschmann, M.M., Frost, D.J., 2003. Highpressure partial melting of garnet pyroxenite: possible mafic lithologies in the source of ocean island basalts. Earth Planet. Sci. Lett. 216, 603–617.

Le Roux, V., Lee, C.-T., Turner, S., 2010. Zn/Fe systematics in mafic and ultramafic systems: implications for detecting major element heterogeneities in the Earth's mantle. Geochim. Cosmochim. Acta 74, 2779–2796.

Lee, C.-T.A., Luffi, P., Plank, T., Dalton, H., Leeman, W.P., 2009. Constraints on the depths and temperatures of basaltic magma generation on Earth and other terrestrial planets using new thermobarometers for mafic magmas. Earth Planet. Sci. Lett. 279, 20–33.

Li, C., Ripley, E.M., 2010. The relative effects of composition and temperature on olivine-liquid Ni partitioning: statistical deconvolution and implications for petrologic modeling. Chem. Geol. 275, 99–104.

Li, X.-H., Li, Z.-X., Zhou, H., Liu, Y., Kinny, P.D., 2002. U–Pb zircon geochronology, geochemistry and Nd isotopic study of Neoproterozoic bimodal volcanic rocks in the Kangdian Rift of South China: implications for the initial rifting of Rodinia. Precambrian Res. 113, 135–154.

Li, C., Tao, Y., Qi, L., Ripley, E.M., 2012. Controls on PGE fractionation in the Emeishan picrites and basalts: constraints from integrated lithophile–siderophile elements and Sr–Nd isotopes. Geochim. Cosmochim. Acta 90, 12–32.

Li, C., Ripley, E.M., Tao, Y., Hu, R., 2016. The significance of PGE variations with Sr–Nd isotopes and lithophile elements in the Emeishan flood basalt province from SW China to northern Vietnam. Lithos 248, 1–11.

Liu, J., Xia, Q.-K., Kuritani, T., Hanski, E., Yu, H.-R., 2017. Mantle hydration and the roleof water in the generation of large igneous provinces. Nat. Commun. 8, 1824.

Lugmair, G.W., Marti, K., 1978. Lunar initial $^{143}Nd/^{144}Nd$: differential evolution of the lunar crust and mantle. Earth Planet. Sci. Lett. 39, 349–357.

Matzen, A.K., Baker, M.B., Beckett, J.R., Stolper, E.M., 2013. The temperature and pressure dependence of nickel partitioning between olivine and silicate melt. J. Petrol. 54, 2521–2545.

Matzen, A.K., Wood, B.J., Baker, M.B., Stolper, E.M., 2017. The roles of pyroxenite and peridotite in the mantle sources of oceanic basalts. Nat. Geosci. 10, 530.

Miyazaki, T., Shuto, K., 1998. Sr and Nd isotope ratios of twelve GSJ rock reference samples. Geochem. J. 32, 345–350.

Palme, H., O'Neill, H.St.C., 2014. Cosmochemical estimates of mantle composition. In: Carlson, R.W. (Ed.), The Mantle and Core, Treatise on Geochemistry, 2nd ed. Elsevier, Amsterdam, pp. 1–39.

Park, J.-W., Campbell, I.H., Eggins, S.M., 2012. Enrichment of Rh, Ru, Ir and Os in Cr spinels from oxidized magmas: evidence from the Ambae volcano, Vanuatu. Geochim. Cosmochim. Acta 78, 28–50.

Pertermann, M., Hirschmann, M.M., 2003. Anhydrous partial melting experiments on MORB-like eclogite: phase relations, phase compositions and mineral-melt partitioning of major elements at 2–3 GPa. J. Petrol. 44, 2173–2201.

Qi, L., Gao, J., Huang, X., Hu, J., Zhou, M.-F., Zhong, H., 2011. An improved digestion technique for determination of platinum group elements in geological samples. J. Anal. Atom. Spectr. 26, 1900–1904.

Ren, Z.-Y., Wu, Y.-D., Zhang, L., Nichols, A.R., Hong, L.-B., Zhang, Y.-H., Zhang, Y., Liu, J.-Q., Xu, Y.-G., 2017. Primary magmas and mantle sources of Emeishan basalts constrained from major element, trace element and Pb isotope compositions of olivine-hosted melt inclusions. Geochim. Cosmochim. Acta 208, 63–85.

Righter, K., Campbell, A., Humayun, M., Hervig, R., 2004. Partitioning of Ru, Rh, Pd, Re, Ir, and au between Cr-bearing spinel, olivine, pyroxene and silicate melts1. Geochim. Cosmochim. Acta 68, 867–880.

Roeder, P.L., Emslie, R., 1970. Olivine-liquid equilibrium. Contrib. Mineral. Petrol. 29, 275–289.

Rudnick, R.L., Gao, S., 2014. Composition of the continental crust. In: Rudnick, R.L. (Ed.), Treatise on Geochemistry, the Crust, 2nd ed. Elsevier, Amsterdam, pp. 1–51.

Schaefer, B.F., Parkinson, I.J., Hawkesworth, C.J., 2000. Deep mantle plume osmium isotope signature from West Greenland Tertiary picrites. Earth Planet. Sci. Lett. 175, 105–118.

Shellnutt, J.G., 2014. The Emeishan large igneous province: a synthesis. Geosci. Front. 5, 369–394.

Shellnutt, J.G., Pham, T.T., 2018. Mantle potential temperature estimates and primary melt compositions and the low-Ti Emeishan flood basalt. Front. Earth Sci. 6, 67. https://doi.org/10.3389/feart.2018.00067.

Shellnutt, J.G., Wang, K.-L., Zellmer, G.F., Iizuka, Y., Jahn, B.-M., Pang, K.-N., Qi, L., Zhou, M.-F., 2011. Three Fe-Ti oxide ore-bearing gabbro-granitoid complexes in the Panxi region of the Permian Emeishan large igneous province, SW China. Am. J. Sci. 311, 773–812.

Shellnutt, J.G., Pham, T.T., Denyszyn, S.W., Yeh, M.W., Tran, T., 2020. Magmatic duration of the Emeishan large igneous province: insight from northern Vietnam. Geology. https://doi.org/10.1130/G47076.1.

Sobolev, A.V., Hofmann, A.W., Kuzmin, D.V., Yaxley, G.M., Arndt, N.T., Chung, S.-L., Danyushevsky, L.V., Elliott, T., Frey, F.A., Garcia, M.O., 2007. The amount of recycled crust in sources of mantle-derived melts. Science 316, 412–417.

Steiger, R.H., Jäger, E., 1977. Subcommission on geochronology: convention on the use of decay constants in geo-and cosmochronology. Earth Planet. Sci. Lett. 36, 359–362.

Tanaka, T., Togashi, S., Kamioka, H., Amakawa, H., Kagami, H., Hamamoto, T., Yuhara, M., Orihashi, Y., Yoneda, S., Shimizu, H., 2000. JNdi-1: a neodymium isotopic reference in consistency with LaJolla neodymium. Chem. Geol. 168, 279–281.

Tao, Y., Putirka, K., Hu, R.-Z., Li, C., 2015. The magma plumbing system of the Emeishan large igneous province and its role in basaltic magma differentiation in a continental setting. Am. Mineral. 100, 2509–2517.

Walter, M.J., 1998. Melting of garnet peridotite and the origin of komatiite and depleted lithosphere. J. Petrol. 39, 29–60.

Xiao, L., Xu, Y., Mei, H., Zheng, Y., He, B., Pirajno, F., 2004. Distinct mantle sources of low-Ti and high-Ti basalts from the western Emeishan large igneous province, SW China: implications for plume–lithosphere interaction. Earth Planet. Sci. Lett. 228, 525–546.

Xu, R., Liu, Y., 2016. Al-in-olivine thermometry evidence for the mantle plume origin of the Emeishan large igneous province. Lithos 266, 362–366.

Xu, Y.-G., Chung, S.-L., Jahn, B.-M., Wu, G., 2001. Petrologic and geochemical constraints on the petrogenesis of Permian–Triassic Emeishan flood basalts in southwestern China. Lithos 58, 145–168.

Xu, Y.-G., He, B., Chung, S.-L., Menzies, M.A., Frey, F.A., 2004. Geologic, geochemical, and geophysical consequences of plume involvement in the Emeishan flood-basalt province. Geology 32, 917–920.

Xu, J.-F., Suzuki, K., Xu, Y.-G., Mei, H.-J., Li, J., 2007. Os, Pb, and Nd isotope geochemistry of the Permian Emeishan continental flood basalts: insights into the source of a large igneous province. Geochim. Cosmochim. Acta 71, 2104–2119.

Xu, R., Liu, Y., Lambart, S., 2020. Melting of a hydrous peridotite mantle source under the Emeishan large igneous province. Earth Sci. Rev. https://doi.org/10.1016/j.earscirev.2020.103253.

Yan, D.-P., Zhou, M.-F., Song, H., Fu, Z., 2003. Structural style and tectonic significance of the Jianglang dome in the eastern margin of the Tibetan Plateau, China. J. Struct. Geol. 25, 765–779.

Yang, Z.-F., Zhou, J.-H., 2013. Can we identify source lithology of basalt? Sci. Rep. 3, 1856.

Yao, J.-H., Zhu, W.-G., Li, C., Zhong, H., Bai, Z.-J., Ripley, E.M., Li, C., 2018. Petrogenesis and ore genesis of the Lengshuiqing magmatic sulfide deposit in Southwest China: constraints from chalcophile elements (PGE, Se) and Sr-Nd-Os-S isotopes. Econ. Geol. 113, 675–698.

Yao, J.-H., Zhu, W.-G., Li, C., Zhong, H., Yu, S., Ripley, E.M., Bai, Z.-J., 2019. Olivine O isotope and trace element constraints on source variation of picrites in the Emeishan flood basalt province, SW China. Lithos 338, 87–98.

Yao, J., Zhang, G., Wang, S., Zhao, J., 2021. Recycling of carbon from the stagnant paleo-Pacific slab beneath Eastern China revealed by olivine geochemistry. Lithos 106249.

Yu, S.-Y., Shen, N.-P., Song, X.-Y., Ripley, E.M., Li, C., Chen, L.-M., 2017. An integrated chemical and oxygen isotopic study of primitive olivine grains in picrites from the Emeishan Large Igneous Province, SW China: evidence for oxygen isotope heterogeneity in mantle sources. Geochim. Cosmochim. Acta 215, 263–276.

Zhang, Z., Mahoney, J.J., Mao, J., Wang, F., 2006. Geochemistry of picritic and associated basalt flows of the western Emeishan flood basalt province, China. J. Petrol. 47, 1997–2019.

Zhang, L., Ren, Z.-Y., Wang, C.Y., 2017. Melt inclusions in the olivine from the Nantianwan intrusion: implications for the parental magma of Ni-Cu-(PGE) sulfide-bearing mafic-ultramafic intrusions of the ~260Ma Emeishan large igneous province (SW China). J. Asian Earth Sci. 134, 72–85.

Zhang, L., Ren, Z.-Y., Handler, M.R., Wu, Y.-D., Zhang, L., Qian, S.-P., Xia, X.-P., Yang, Q., Xu, Y.-G., 2019. The origins of high-Ti and low-Ti magmas in large igneous provinces, insights from melt inclusion trace elements and Sr-Pb isotopes in the Emeishan large Igneous Province. Lithos 344, 122–133.

Zhong, H., Zhu, W.-G., 2006. Geochronology of layered mafic intrusions from the Pan–Xi area in the Emeishan large igneous province, SW China. Mineral. Deposita 41, 599–606.

Zhong, H., Zhou, X.-H., Zhou, M.-F., Sun, M., Liu, B.-G., 2002. Platinum-group element geochemistry of the Hongge Fe–V–Ti deposit in the Pan-Xi area, southwestern China. Mineral. Deposita 37, 226–239.

Zhong, H., Campbell, I.H., Zhu, W.-G., Allen, C.M., Hu, R.-Z., Xie, L.-W., He, D.-F., 2011. Timing and source constraints on the relationship between mafic and felsic intrusions in the Emeishan large igneous province. Geochim. Cosmochim. Acta 75, 1374–1395.

Zhong, Y., Mundil, R., Chen, J., Yuan, D., Denyszyn, S.W., Jost, A.B., Payne, J.L., He, B., Shen, S., Xu, Y., 2020. Geochemical, biostratigraphic, and high-resolution geochronological constraints on the waning stage of Emeishan Large Igneous Province. Geol. Soc. Am. Bull. https://doi.org/10.1130/B35464.1.

Zhou, M.-F., Arndt, N.T., Malpas, J., Wang, C.Y., Kennedy, A.K., 2008. Two magma series and associated ore deposit types in the Permian Emeishan large igneous province, SW China. Lithos 103, 352–368.

Zhu, W.-G., Zhong, H., Deng, H.-L., Wilson, A., Liu, B.-G., Li, C.-Y., Qin, Y., 2006. SHRIMP zircon U-Pb age, geochemistry, and Nd-Sr isotopes of the Gaojiacun mafic-ultramafic intrusive complex, Southwest China. Int. Geol. Rev. 48, 650–668.

Zhu, W.-G., Zhong, H., Li, X.-H., Deng, H.-L., He, D.-F., Wu, K.-W., Bai, Z.-J., 2008. SHRIMP zircon U–Pb geochronology, elemental, and Nd isotopic geochemistry of the Neoproterozoic mafic dykes in the Yanbian area, SW China. Precambrian Res. 164, 66–85.

Zindler, A., Hart, S., 1986. Chemical geodynamics. Annu. Rev. Earth Planet. Sci. 14, 493–571.